

# Mapping the radiative and non-radiative local density of states in the near-field of a gold nanoantenna

D. Cao,<sup>1</sup> A. Cazé,<sup>1</sup> M. Calabrese,<sup>1</sup> R. Pierrat,<sup>1</sup> N. Bardou,<sup>2</sup> S. Collin,<sup>2</sup> R. Carminati,<sup>1</sup> V. Krachmalnicoff,<sup>1,\*</sup> and Y. De Wilde<sup>1</sup>

<sup>1</sup>*Institut Langevin, ESPCI ParisTech, CNRS, 1 rue Jussieu, 75238 Paris Cedex 05, France*

<sup>2</sup>*Laboratoire de Photonique et Nanostructures (LPN-CNRS), Route de Nozay, 91460 Marcoussis, France*

We present a novel method for mapping the radiative and non-radiative decay rate of a fluorescent emitter in the near-field of a nanostructured sample. The approach is based on the simultaneous mapping of the fluorescence intensity and decay rate and on the rigorous application of the reciprocity theorem. Data analysis is based on an analytical calculation which is detailed in the paper. Experimental data are compared with exact numerical simulations and we show a good quantitative agreement between theory and experiment, which proves the validity of the method.

PACS numbers: 78.67.-n, 07.79.Fc, 42.25.Bs, 33.50.-j

Tailoring light-matter interaction is a key issue in modern photonics. A full control of such interaction on the nanometer scale can have a huge impact in a wide range of domains, going from fundamental physics (e.g. control of spontaneous emission with optical antennas [1–3], strong coupling [4–7], cavity quantum electrodynamics with localized modes [8–10]) to the design of novel devices (e.g. light harvesting [11, 12], photon detection [13], biological sensing [14]). A measurement of light-matter coupling is given by the Purcell factor, which describes the enhancement of the spontaneous decay rate of an emitter in a given environment. It has been known since the pioneering work by Drexhage [15] that the decay rate is modified in the vicinity of a metallic structure. However, one can observe an enhancement of either the radiative decay rate (corresponding to photon emission in the far field) or the non-radiative decay rate (which measures the coupling to dark modes and absorption losses)[16]. Depending on the targeted application (e.g. the design of an efficient single photon source or an efficient quencher of molecular fluorescence), it can be interesting to enhance either the radiative or the non-radiative decay rate. Therefore, measuring both decay rates is a crucial issue in the characterization of nanostructures dedicated to the control of light-matter interaction. Despite the broad interest, such a measurement has remained challenging and only a few experiments have been reported [17–19], that only partially address the issue.

In this Letter we present a new approach for the mapping of the radiative and non-radiative decay rates using a fluorescent nanosource scanned in the near-field of a metallic nanoantenna. The fluorescent scanning probe allows us to map simultaneously the fluorescence intensity and decay rate, which is proportional to the local density of states (LDOS) [20], in a confocal geometry in which excitation and detection paths coincide exactly. This allows us to apply rigorously the reciprocity theorem to separate the radiative and non-radiative contributions, as will be shown by an analytical calculation. The

method properly accounts for the radiation pattern of the observed antenna. In order to check the validity of the proposed method, we compare the results obtained from the measurements with an exact numerical simulation.

The fluorescence intensity emitted by a dipole located in the near-field of a metallic nanostructure depends on two processes. (1) The change of the exciting field at the position of the emitter induced by the local environment. (2) The balance between the radiative and the non-radiative decay rates, that also depends on the environment. For a dipole located at  $\mathbf{r}_0$ , the fluorescence intensity can be written as:

$$I_{fluo}(\mathbf{r}_d) = A \frac{\Gamma_{1,\Omega}^R}{\Gamma_1} \sigma_{abs} I_{exc}(\mathbf{r}_0) \quad (1)$$

where  $\mathbf{r}_d$  is the position of the detector,  $\Gamma_1$  is the total decay rate,  $\Gamma_{1,\Omega}^R = \int_{\Omega_d} \Gamma_1^R(\mathbf{u}) d\Omega_d$  is the radiative decay rate integrated over the detection solid angle  $\Omega_d$  ( $\mathbf{u}$  being a unit vector defining a detection direction),  $I_{exc}(\mathbf{r}_0)$  is the local excitation intensity and  $\sigma_{abs}$  is the absorption cross-section.  $A$  is a constant that takes into account the detection efficiency and photon losses along the optical path to the detector. In the exact confocal geometry considered in this work, exciting and detected photons follow the same path (see Fig. 1). The reciprocity theorem [21, 22] states that  $\mathbf{u}_1 \cdot \mathbf{E}_{exc}(\mathbf{r}_0) = \mathbf{u}_d \cdot \mathbf{E}_{fluo}(\mathbf{r}_d)$  where  $\mathbf{u}_1$  is the unit vector along the direction of the transition dipole of the emitter,  $\mathbf{u}_d$  is a unit vector defining a polarization direction at the detector,  $\mathbf{E}_{exc}(\mathbf{r}_0)$  is the exciting field and  $\mathbf{E}_{fluo}(\mathbf{r}_d)$  is the field reaching the detector. Therefore, for a polarized detection along  $\mathbf{u}_d$ :

$$\Gamma_{1,\Omega}^R = B |\mathbf{u}_d \cdot \mathbf{E}_{fluo}(\mathbf{r}_d)|^2 = B |\mathbf{u}_1 \cdot \mathbf{E}_{exc}(\mathbf{r}_0)|^2 = B I_{exc}(\mathbf{r}_0) \quad (2)$$

where  $B$  is a constant. Note that Eq. (2) is valid at a specific wavelength. In practice, it can be applied provided that the response of the nanoantenna is broadband compared to the Stokes shift of the molecule. Inserting Eq. (2) into Eq. (1), and summing over all possible

dipole orientations  $\mathbf{u}_1$  and field polarizations  $\mathbf{u}_d$ , we end up with an expression for the total detected fluorescence intensity:

$$I_{fluo}^{tot}(\mathbf{r}_d) = \frac{A}{B} \sigma_{abs} \left[ \frac{(\Gamma_{1,\Omega}^R)^2}{\Gamma_1} + \frac{(\Gamma_{2,\Omega}^R)^2}{\Gamma_2} + \frac{(\Gamma_{3,\Omega}^R)^2}{\Gamma_3} \right] \quad (3)$$

where the subscripts (1, 2, 3) refer to three orthogonal directions of the transition dipole. This expression directly connects the detected fluorescence intensity to the total and the radiative decay rate. It is an essential relationship in the method described in this Letter, as we shall see in the analysis of the experimental data.

The simultaneous mapping of the LDOS and fluorescence intensity has been reported [20, 23]. The experimental setup used here is based on a configuration previously developed by some of the authors [20] with the major difference that the excitation and detection paths are rigorously the same, as sketched in Fig.1.

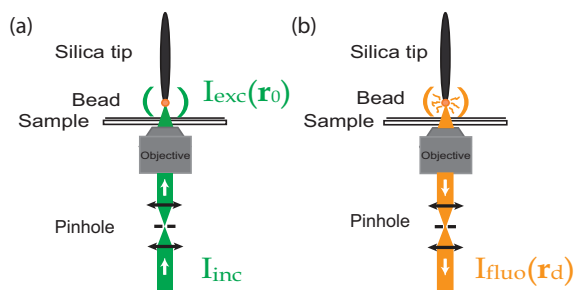


FIG. 1: Simplified sketch of the experimental setup. (a) Excitation path. (b) Detection path.

The sample is mounted on a sample-scanning inverted confocal microscope combined with a homebuilt atomic force microscope (AFM). The AFM tip is a tapered optical fiber. A fluorescent bead (Invitrogen Red Fluospheres, diameter 100 nm) is grafted at the extremity of the tip of the AFM. The excitation is performed at 560 nm through a 150  $\mu\text{m}$  confocality pinhole and an oil objective (N.A. 1.4) with a supercontinuum pulsed laser (Fianium SC450) at a repetition rate of 10 MHz. Fluorescence photons are collected through the same objective, pass in the confocality pinhole and then are separated from the exciting photons with a dichroic mirror and a high-pass filter ( $\lambda > 594$  nm). Importantly, the use of the same confocal pinhole on the excitation and detection optical paths, ensures that excitation/detection photons are emitted/detected through the same optical mode. This is crucial for the application of the reciprocity theorem.

Time-resolved photon detection is performed with a time correlated single photon counting system (Picoquant HydraHarp 400), which allows one to simultaneously map the fluorescence intensity and decay rate. The fluorescent scanning probe is held by shear force feedback at a constant distance of approximately 20 nm to

the surface of a nanostructured sample while the latter is scanned. The topography of the sample is recorded simultaneously with the decay rate (LDOS) and fluorescence intensity maps.

We present the study of two different nanostructures, obtained by electron beam lithography on a glass substrate: a single 130 nm diameter and 30 nm thick gold disc (monomer), and a linear chain of three 130 nm diameter gold nanodiscs separated by 20 nm gaps (trimer).

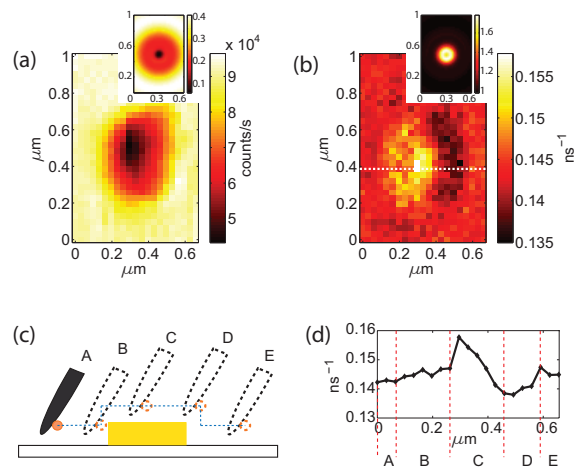


FIG. 2: (a) Fluorescence intensity map for one gold nanodisc. (b) Decay rate map for the same gold nanodisc. Insets: numerically calculated maps. The decay rate map has been normalised by its value in vacuum. (c) Path followed by the fluorescent probe during the scan (not to scale). (d) Cross section through the row indicated with a white dashed line in (b).

Figures 2(a,b) show the fluorescence intensity and decay rate maps for the gold monomer. The intensity map has been corrected for a slow progressive lateral drift of the fluorescent probe with respect to the exciting laser beam (on the order of 3 nm per minute), which results in a progressive decrease of the mean intensity detected during the scan. We therefore start the data analysis process by subtracting a gradient background from the intensity map and by adding an offset corresponding to the mean value of the background. This processing does not affect the LDOS map. As confirmed by numerical simulations shown in the insets of Fig. 2, we observe an increase of the LDOS and a decrease of the fluorescence intensity in correspondence with the metallic structure. The contrast of the numerical maps is overestimated due to the absence of the substrate in the simulation. The experimental LDOS map shows a zone where the LDOS has a smaller value than on the glass substrate, and a zone where it has an intermediate value between that on the glass substrate and that on the gold disc. This behaviour is due to a grafting of the fluorescent bead on

the side of the silica tip, as depicted in Fig. 2(c). Figure 2(d) shows the profile of the decay rate along the white dashed line in Fig. 2(b). At the beginning of the scan (zone A in Fig. 2(c,d)), both the tip and the bead are at a given height on the glass coverslip. As the tip approaches the nanodisc (zone B), the bead gets closer to the gold disc and the LDOS slowly increases. Then both the tip and the bead are scanned on top of the disc and the bead feels an enhanced LDOS (zone C). Approaching the disc edge, the tip remains on the disc, while the bead is driven out of it (zone D). In this position the bead feels a reduced LDOS compared to that on the glass coverslip because of the larger glass-bead distance (on the order of 50 nm). Finally, both the tip and the bead are scanned over the glass coverslip (zone E) and the bead feels the same LDOS as in the initial position. Note that we have checked that the value of the decay rate measured in zone D is the same as that measured when the tip is retracted by 30 nm above the bare glass coverslip.

In order to extract the radiative and non-radiative decay rate maps from the experimental data, we proceed as follows. Since the fluorescent bead contains several thousands molecules with random orientations, we are not able to measure the ratio  $\Gamma_{i,\Omega}^R/\Gamma_i$  in the three directions of the transition dipole. We introduce an LDOS anisotropy factor  $C = \Gamma/\Gamma_i$  and assume an isotropic response of the system. The relevance of such an assumption will be checked afterward by comparison with numerical simulations. In these conditions, Eq. (3) can be rewritten as:

$$I_{fluo}^{tot}(\mathbf{r}_d) = 3 \frac{AC}{B} \sigma_{abs} \frac{(\Gamma_{rms,\Omega}^R)^2}{\Gamma} \quad (4)$$

where

$$\Gamma_{rms,\Omega}^R = \left[ \frac{(\Gamma_{1,\Omega}^R)^2 + (\Gamma_{2,\Omega}^R)^2 + (\Gamma_{3,\Omega}^R)^2}{3} \right]^{1/2} \quad (5)$$

is the effective radiative decay rate that we extract from the experimental data. In order to deduce  $\Gamma_{rms,\Omega}^R$  from the measurement of  $I_{fluo}^{tot}(\mathbf{r}_d)$  and the total decay rate  $\Gamma$ , we have to get rid of the unknown prefactor in Eq. (4). This is done by measuring the fluorescence intensity and the decay rate with the same bead, excited with the same laser power but on a bare glass substrate used as a reference sample. In practice, we use the values of the intensity and decay rate on the first pixel of the maps (i.e. far from the gold structure). Since the non-radiative component of the decay rate is negligible on this reference sample, the reference fluorescence intensity is given by  $I_{fluo}^{ref}(\mathbf{r}_d) = 3(AC/B)(\Omega/4\pi)^2 \sigma_{abs} \Gamma_{ref}$ . This allows us to rewrite Eq. (4) in the form

$$I_{fluo}^{tot}(\mathbf{r}_d) = \left( \frac{4\pi}{\Omega} \right)^2 \frac{I_{fluo}^{ref}(\mathbf{r}_d)}{\Gamma_{ref}} \frac{(\Gamma_{rms,\Omega}^R)^2}{\Gamma}. \quad (6)$$

Note that we consider that the constant  $C$  is the same on the reference and the real sample, an assumption whose relevance will also be assessed through the comparison with numerical simulations.

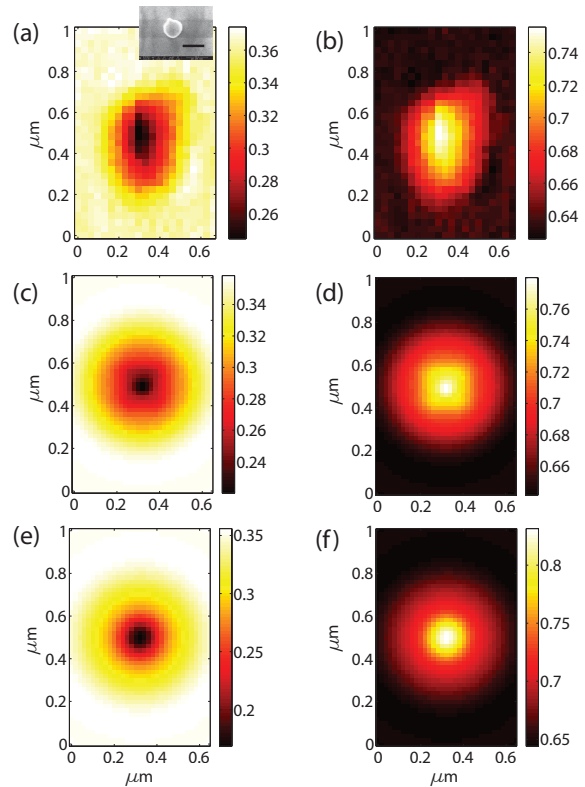


FIG. 3: (a,b) Measured effective radiative  $\Gamma_{rms,\Omega}^R$  and non-radiative  $\Gamma_{rms,\Omega}^{NR}$  map for a single gold nanodisc, normalized by the measured total decay rate map. Inset: SEM image of the sample, black bar: 200 nm. (c,d) Numerical maps of the effective radiative decay rate  $\Gamma_{rms,\Omega}^R$  and non-radiative decay rate  $\Gamma_{rms,\Omega}^{NR}$  normalized by the calculated total decay rate map. (e,f) Numerical maps of the real radiative decay rate  $\Gamma_{\Omega}^R$  and non-radiative decay rate  $\Gamma_{\Omega}^{NR}$  normalized by the calculated total decay rate map.

The map of the effective radiative decay rate  $\Gamma_{rms,\Omega}^R$  in the near-field of the gold monomer, as deduced from the experimental data, is shown in Fig. 3(a). The map of the effective non-radiative decay rate, defined by  $\Gamma_{rms,\Omega}^{NR} = \Gamma - \Gamma_{rms,\Omega}^R$ , is shown in Fig. 3 (b). This non-radiative decay rate includes the contributions of absorption losses, and of photon losses due to radiation out of the detection solid angle. Both effective radiative and non-radiative decay rates maps have been normalized by the total decay rate map shown in Fig. 2(b).

In order to get insight into the experimental results, and to assess the validity of the two hypotheses made in the procedure for the data analysis, we have performed numerical simulations using the method described in Refs. [20, 25]. The calculation of the electric field is based

on the volume integral equation

$$\mathbf{E}(\mathbf{r}) = \mathbf{E}_0(\mathbf{r}) + k_0^2 \int_V [\epsilon(\omega) - 1] \mathbf{G}_0(\mathbf{r}, \mathbf{r}', \omega) \mathbf{E}(\mathbf{r}') d\mathbf{r}', \quad (7)$$

where  $k_0 = \omega/c$ , with  $c$  the speed of light in vacuum,  $V$  is the volume occupied by gold,  $\mathbf{E}_0$  is the incident field,  $\mathbf{G}_0$  is the dyadic Green function of the host medium (vacuum in our simulations) and  $\epsilon(\omega)$  is the dielectric function of gold, taken from Ref. [26]. Equation (7) is solved by a moment method [27], where the Green function  $\mathbf{G}_0$  is integrated over the discretization cells (2.5 nm cubic cells) to improve convergence [28]. Solving Eq. (7) under illumination by a plane wave (excitation stage) or an electric dipole source (emission stage) allows us to compute the total electric field  $\mathbf{E}$  (or equivalently the total Green function  $\mathbf{G}$ ) everywhere, and to deduce all the parameters entering the fluorescence decay rates and intensity. The total decay rate is deduced from  $\Gamma(\mathbf{r}_0, \omega)/\Gamma_0 = (2\pi/k_0) \text{Im Tr} [\mathbf{G}(\mathbf{r}_0, \mathbf{r}_0, \omega)]$ , where  $\Gamma_0$  is the decay rate in vacuum and  $\text{Tr}$  denotes the trace of a tensor. The radiative decay rate  $\Gamma_{i,\Omega}^R(\omega_{fluo})$  integrated over the detection solid angle, for a given orientation  $i$  of the transition dipole, can be computed from the far-field radiation pattern at the emission frequency  $\omega_{fluo}$  [25]. The excitation intensity  $I_{exc}(\mathbf{r}_0)$  is calculated using a plane-wave illumination at normal incidence and at the excitation frequency  $\omega_{exc}$ . The calculation is averaged over two orthogonal polarizations to mimic the unpolarized laser used in the experiment. Excitation and emission wavelengths are set to 560 nm and 605 nm respectively.

In order to directly compare simulations and experiments, we have calculated the effective radiative decay rate  $\Gamma_{rms,\Omega}^R$  and non-radiative decay rate  $\Gamma_{rms,\Omega}^{NR}$ . The simulated maps, normalized by the calculated total decay rate map, are shown in Fig. 3(c,d). Numerical simulations and experiments are in good quantitative agreement. This proves that the assumptions made in the theoretical model used to extract the effective radiative decay rate from the measurement of the total decay rate and the fluorescence intensity are relevant.

In order to further check the relevance of the analysis, we also compared the effective decay rate maps with the real values of the radiative decay rate and of the non-radiative decay rate (defined as the difference between the total decay rate and the radiative decay rate integrated over the solid angle) obtained from the numerical simulation. The corresponding maps are shown in Fig. 3(e,f). The agreement between theory and experiment remains very good, proving the robustness of the effective parameters deduced from the experimental data as estimates of the real radiative and non-radiative decay rates.

The method described above can be applied to more complex systems. As an example, we have determined the effective radiative decay rate  $\Gamma_{rms,\Omega}^R$  and non-

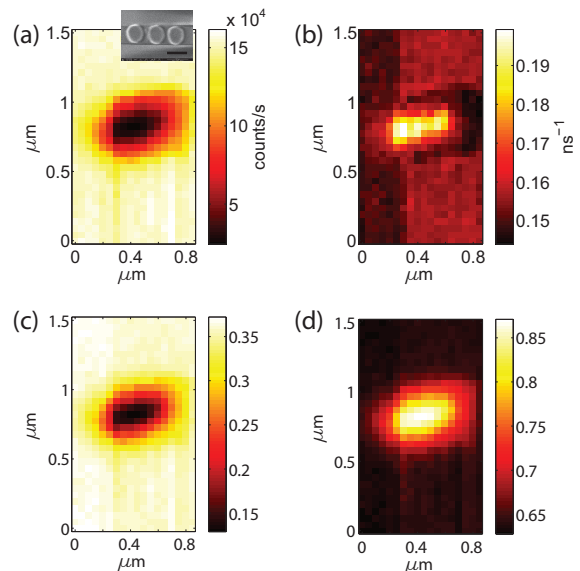


FIG. 4: (a) Fluorescence intensity map, (b) decay rate map, (c) normalized effective radiative decay rate map  $\Gamma_{rms,\Omega}^R/\Gamma$  and (d) normalized effective non-radiative decay rate map  $\Gamma_{rms,\Omega}^{NR}/\Gamma$  of a linear chain of three gold nanodiscs. Inset: SEM image of the sample, black bar: 200 nm.

radiative decay rate  $\Gamma_{rms,\Omega}^{NR}$  on an optical antenna formed by three gold discs (trimer) of diameter 130 nm separated by two gaps of 20 nm. The experiment has been performed with the same fluorescent probe as for the monomer, and the resulting data are shown in Fig. 4. As expected, the data show a decrease of the fluorescence intensity in correspondence with an increase of the LDOS when the bead is on the top of the nanostructure. Similarly to the case of the monomer, the LDOS map exhibits a region on the right of the trimer with a reduced value, whose origin can be explained using the argument depicted in Fig. 2(c). Since the fluorescence intensity is much less sensitive to the bead-sample distance than the LDOS, this signature of the probe asymmetry artefact is not visible in the intensity map. The effective radiative and non-radiative decay rate maps, obtained using the procedure described above and normalized by the measured total decay rate map, are shown in Fig. 4(c,d). As in the case of the gold monomer, the non-radiative decay rate is larger than the radiative decay rate, by about a factor of two. This is, to our knowledge, the first quantitative characterization of the radiative and non-radiative properties of a structured optical antenna.

In conclusion, we have introduced an experimental method to map the radiative and non-radiative local density of photonic states which is crucial for the study and the characterization of nanostructured samples for a wide range of applications. The key point is the simultaneous measurement of the fluorescence intensity and decay rate in an exact confocal geometry, permitting a rigorous use

of the reciprocity theorem. In the case of a single gold nanodisc, the experimental procedure is in quantitative agreement with exact numerical simulations, thus proving the relevance of the approach. The general applicability of the method has been demonstrated by mapping for the first time the radiative and non-radiative local density of states on a more complex optical antenna but it could also be applied to other metallic or dielectric nanostructures.

We acknowledge Abdel Souilah for technical support. This work was supported by LABEX WIFI (Laboratory of Excellence within the French Program “Investments for the Future”) under reference ANR-10-IDEX-0001-02 PSL\* and by the Region Ile-de-France in the framework of DIM Nano-K.

---

\* Electronic address: valentina.krachmalnicoff@espci.fr

- [1] S. Kühn, U. Hakanson, L. Rogobete and V. Sandoghdar, *Phys. Rev. Lett.* **97**, 017402 (2006).
- [2] P. Anger, P. Bharadwaj and L. Novotny, *Phys. Rev. Lett.* **96**, 113002 (2006).
- [3] M. Frimmer, and A. F. Koenderink, *Phys. Rev. Lett.* **110**, 217405 (2013).
- [4] D. E. Chang, A. S. Sorensen, P. R. Haemmer, and M. D. Lukin, *Phys. Rev. Lett.* **97**, 053002 (2006).
- [5] D. E. Chang, A. S. Sorensen, E. A. Demler, and M. D. Lukin, *Nat. Phys.* **3**, 807812 (2007).
- [6] P. Vasa, W. Wang, R. Pomraenke, M. Lammers, M. Maiuri, C. Manzoni, G. Cerullo, and C. Lienau, *Nat. Phot.* **7**, 128 (2013).
- [7] S. Aberra Guebrou, C. Symonds, E. Homeyer, J. Plenat, Y. Gartstein, V. Agranovich, and J. Bellessa, *Phys. Rev. Lett.* **108**, 066401 (2012).
- [8] P. Michler, A. Kiraz, C. Becher, W. V. Schoenfeld, P. M. Petroff, Lidong Zhang, E. Hu and A. Imamoglu, *Science* **290**, 2282 (2000).
- [9] L. Sapienza, H. Thyrestrup, S. Stobbe, P. D. Garcia, S. Smolka, and P. Lodahl, *Science* **327**, 1352 (2010).
- [10] A. Cazé, R. Pierrat, and R. Carminati, *Phys. Rev. Lett.* **111**, 053901 (2013).
- [11] J. A. Schuller, E. S. Barnard, W. Cai, Y. Chul Jun, J. S. White, and M. L. Brongersma, *Nat. Mater.* **9**, 193 (2010).
- [12] H. A. Atwater, and A. Polman, *Nat. Mater.* **9**, 205 (2010).
- [13] G. Konstantatos, and E. H. Sargent, *Nature Nanotech.* **5**, 391 (2010).
- [14] J. Homola, *Chem. Rev.* **108**, 462 (2008).
- [15] K. Drexhage, *J. Lumin.* **1**, 693 (1970).
- [16] R. Carminati, J.-J. Greffet C. Henkel and J.M. Vigoureux, *Opt. Commun.* **261**, 368 (2006).
- [17] J. N. Farahani, D. W. Pohl, H. -J. Eisler, and B. Hecht, *Phys. Rev. Lett.* **95**, 017402 (2005)
- [18] X. Brokmann, L. Coolen, M. Dahan, and J. P. Hermier, *Phys. Rev. Lett.* **93**, 107403 (2004).
- [19] B. C. Buchler, T. Kalkbrenner, C. Hettich, and V. Sandoghdar, *Phys. Rev. Lett.* **95**, 063003 (2005).
- [20] V. Krachmalnicoff, D. Cao, A. Cazé, E. Castanié, R. Pierrat, N. Bardou, S. Collin, R. Carminati and Y. De Wilde, *Optics Express*, 11540 (2013).
- [21] R. Carminati, J.-J. Greffet and M. Nieto-Vesperinas, *J. Opt. Soc. Am. A* **15**, 706 (1998).
- [22] L. Novotny, and N. Van Hulst, *Nat. Phot.* **5**, 83 (2011).
- [23] M. Frimmer, Y. Chen and A.F. Koenderink, *Phys. Rev. Lett.* **107**, 123602 (2011).
- [24] L. Novotny and B. Hecht, *Principles of Nano-Optics* (Cambridge University, 2006).
- [25] A. Cazé, R. Pierrat and R. Carminati, *Phot. Nano. Fund. Appl.* **10**, 339 (2012).
- [26] E. D. Palik, *Handbook of Optical constants of solids, Academic Press, San Diego, USA* (1998).
- [27] R.F. Harrington, *Field Computations by Moment Methods, IEEE Press, New York, USA* (1992).
- [28] P.C. Chaumet, A. Sentenac, A. Rahmani, *Phys. Rev. E* **70**, 036606 (2004).